Broadband excitation spectrum of bulk crystals and thin layers of $PtTe_2$

Barun Ghosh,[1] Francesca Alessandro,[2,3] Marilena Zappia,[2] Rosaria Brescia,[4] Chia-Nung Kuo,[5] Chin Shan Lue,[5] Gennaro Chiarello,[2] Antonio Politano,[6,7] Lorenzo S. Caputi,[2] Amit Agarwal,[1,*] and Anna Cupolillo[2,†]

[1]*Department of Physics, Indian Institute of Technology Kanpur, Kanpur 208016, India*
[2]*Department of Physics, University of Calabria, via ponte Bucci, cubo 31/C 87036, Rende (CS), Italy*
[3]*INFN, Sezione LNF, Gruppo Collegato di Cosenza, Cubo 31C, I-87036 Rende (CS), Italy*
[4]*Electron Microscopy Facility, Istituto Italiano di Tecnologia, Via Morego 30, 16163 Genova, Italy*
[5]*Department of Physics, National Cheng Kung University, 1 Ta-Hsueh Road, 70101 Tainan, Taiwan*
[6]*Istituto Italiano di Tecnologia, Graphene Labs via Morego, 30 16163 Genova, Italy*
[7]*Dipartimento di Scienze Fisiche e Chimiche (DSFC), Universita dell'Aquila, Via Vetoio 10, I-67100 L'Aquila, Italy*

(Received 27 August 2018; published 9 January 2019)

We explore the broadband excitation spectrum of bulk $PtTe_2$ using electron energy-loss spectroscopy and density-functional theory. In addition to infrared modes related to intraband three-dimensional (3D) Dirac plasmon and interband transitions between the 3D Dirac bands, we observe modes at 3.9, 7.5, and 19.0 eV in the ultraviolet region. The comparison of the excitation spectrum with the calculated orbital-resolved density of states allows us to ascribe spectral features to transitions between specific electronic states. Additionally, we study the thickness dependence of the high-energy-loss peak in the $PtTe_2$ thin films. We show that, unlike graphene, the high-energy EELS peak in $PtTe_2$ thin film gets redshifted by $\sim$2.5 eV with increasing thickness.

DOI: 10.1103/PhysRevB.99.045414

I. INTRODUCTION

Recently, the PtX_2 (X = Se, Te, S) class of transition-metal dichalcogenides (TMDCs) has attracted a huge interest from the scientific community. This class of TMDCs combines promising application capabilities along with the fundamental physics interest arising from the existence of topological type-II Dirac fermions [1–9]. As opposed to type-I Dirac materials, which have a closed Fermi surface with either an electron or a hole pocket, type-II Dirac materials have an unbounded Fermi surface with both electron and hole pockets [3]. The presence of a bulk topological Dirac node leads to the existence of surface states as well. These surface states are robust against perturbations and have interesting physical properties [10,11].

Thin layers of the PtX_2 class of materials are equally interesting because of their relatively higher mobility, and superior gas sensing properties, among others [2,12–16]. The quantum confinement effect dramatically changes the properties of the thin layers of $PtTe_2$ which undergo a metal-semiconductor transition with decreasing thickness [17,18]. Apart from this, the monolayer exhibits a unique property: because of the local dipole-induced Rashba effect, opposite spins with the same energy get spatially separated on opposite sides of the monolayer [19]. This is known as spin layer locking and it can have potential applications in electrically tunable spintronic devices.

Preceding discussions made it clear that the PtX_2 class of materials has emerged as promising for future electronics. While the band structure of $PtTe_2$ has been explored comprehensively [5], along with the Dirac plasmons (collective density excitations) in the infrared range of the electromagnetic spectrum [20], the high-energy excitations in $PtTe_2$ still remain unexplored. The comprehension of the excitation spectrum of collective modes in the visible-ultraviolet range is crucial to devise broadband photodetectors [21,22], ultraviolet-imaging applications [23], and broadband plasmonic devices [24,25]. Monolayer $PtTe_2$ has the smallest energy band gap in the PtX_2 class of materials [26], offering it an advantage over the other members for applications in nanoelectronics.

Motivated by this, in this paper we probe the broadband excitation spectrum of bulk crystals and thin layers of $PtTe_2$, using electron energy-loss spectroscopy (EELS) [27] complemented by detailed *ab initio* calculations. EELS probes the broadband dielectric response of the system to a negatively charged probe, allowing for spectral contributions from both plasmonic modes and nonvertical transitions from valence-band to conduction-band electronic states. Therefore, EELS investigations supplement the studies of the absorption and emission processes of TMDCs in the long-wavelength limit [28] involving only vertical transitions from occupied to unoccupied states. The nature of various experimentally probed EELS excitations is identified by means of calculations of the band structure and the loss function based on density-functional theory (DFT). In addition to the bulk excitation spectrum, we also explore the changes in the broadband excitation spectrum of $PtTe_2$ on reducing its thickness to few layers. Contrarily to the case of graphene

*amitag@iitk.ac.in
†anna.cupolillo@fis.unical.it

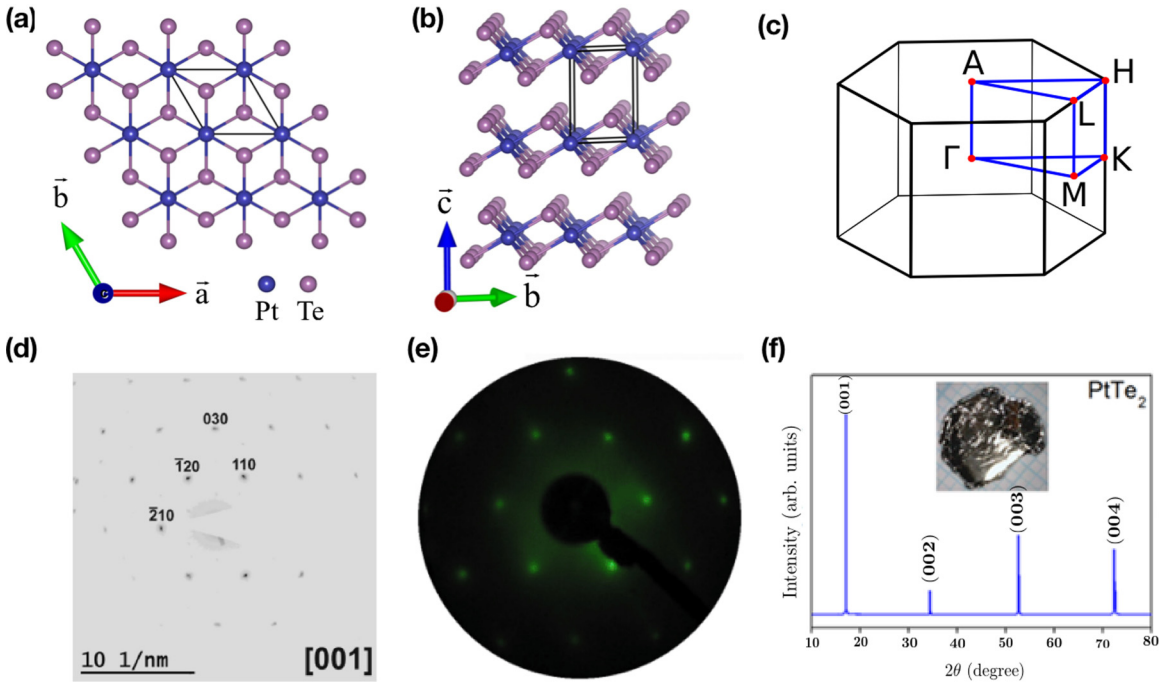

FIG. 1. Panels (a) and (b) show the top and side views of the atomic crystal structure of $PtTe_2$. The corresponding bulk Brillouin zone of the hexagonal $PtTe_2$ crystal, along with various high-symmetry points is shown in (c). (d) SAED patterns acquired on $PtTe_2$ flakes match with [0001]-oriented single-crystal trigonal $PtTe_2$ (ICSD No. 41373, moncheite). (e) LEED pattern of bulk $PtTe_2$ single crystal oriented along the (0001) direction. (f) XRD pattern of (0001)-oriented planes of $PtTe_2$. Only (00n) peaks are observed.

and phosphorene, a blueshift of the high-energy EELS peak frequency is observed for thin layers compared to the bulk [29–31].

The paper is organized as follows: in Sec. II we briefly describe the crystal structure and experimental details related to the growth and characterization of $PtTe_2$ along with that of reflection EELS. This is followed by a discussion of the theoretical *ab initio* calculation of the EELS spectrum and other computational details in Sec. III. The broadband EELS spectrum of bulk $PtTe_2$ is discussed in Sec. IV, followed by the discussion of the excitation spectrum of thin layers in Sec. V. Finally, we summarize our findings in Sec. VI.

II. GROWTH, CRYSTAL STRUCTURE, CHARACTERIZATION, AND DETAILS OF EELS

A. Growth

Single crystals of $PtTe_2$ were prepared by the self-flux method. High-purity Pt (99.99%) foil and Te ingot (99.9999%) were mixed in the ratio of 1:17 and wrapped in a quartz tube under vacuum. The quartz tube was heated to 1000 °C, dwelled there for 8 h, and slowly cooled at a rate of 3–5°C/h to 500 °C. Successively, the excess Te flux was separated by centrifugation. The resulting crystals have typical dimensions of $8 \times 8 \times 1$ mm [13] with the c axis perpendicular to the plates and can be easily cleaved. The structure of the grown crystals was examined by x-ray diffraction (Bruker D2 PHASER) using Cu $K\alpha$ radiation and Laue diffraction at room temperature.

Thin flakes of $PtTe_2$ were obtained by liquid-phase exfoliation of bulk $PtTe_2$ in *N*-methylpyrrolidone.

B. Crystal structure

Bulk $PtTe_2$ belongs to the large family of 1T-metal dichalcogenides with CdI_2-type crystal structure [space group $P\bar{3}m1(164)$]. The bulk structure can be viewed as a collection of isolated monolayers stacked in the out-of-plane direction [see Figs. 1(a) and 1(b)]. In each of these monolayers there are three sublayers, Te-Pt-Te, where the central Pt atom is strongly bonded with six neighboring Te atoms forming a hexagonal honeycomb structure. Both selected-area electron diffraction (SAED) and low-energy electron diffraction (LEED) patterns shown in Figs. 1(d) and 1(e) match with [0001]-oriented flakes and bulk $PtTe_2$, respectively. This orientation is the one characterizing most of the regions probed by transmission electron microscopy (TEM) and used to extract information for the current work. Correspondingly, the x-ray diffraction (XRD) pattern only exhibits (00n) peaks as shown in Fig. 1(f).

C. Characterization

To demonstrate cleanliness, the surface of the single crystal has been characterized by means of vibrational spectroscopy and x-ray photoelectron spectroscopy, without finding any contamination. Once prepared in ultrahigh vacuum, the surface remains uncontaminated for a timescale of several weeks, thus ensuring sample stability. The LEED pattern shows sharp spots against a low background [see Fig. 1(e)].

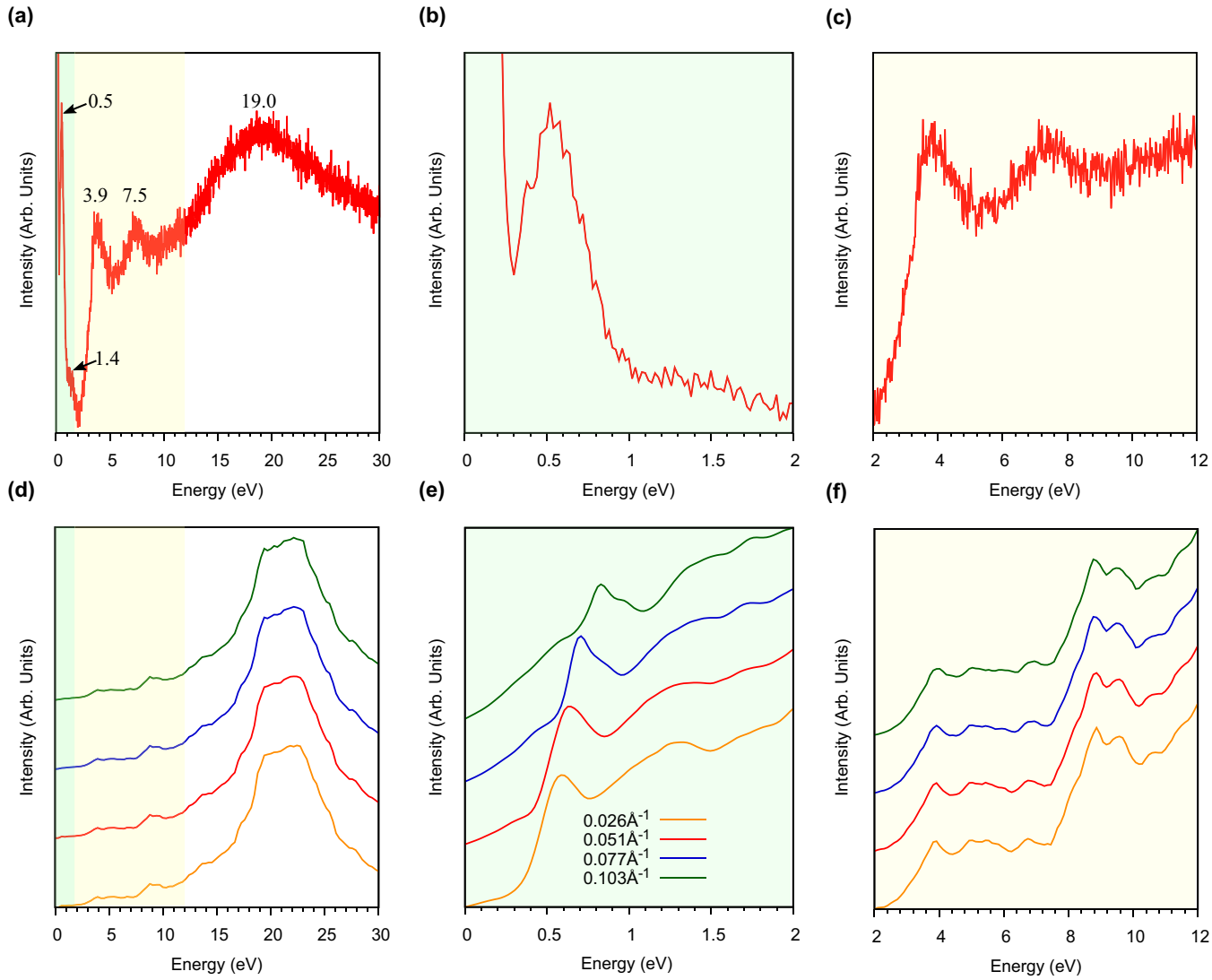

FIG. 2. (a) Broadband EELS spectrum for bulk $PtTe_2$ measured in reflection mode with a primary electron beam energy of 100 eV. The EELS spectrum shows several distinct peaks at energies 0.5, 1.4, 3.9, 7.5, and 19.0 eV, which are highlighted in (b) and (c). The peak at 0.5 eV is dispersive and it is associated with the intraband density excitations [20] in $PtTe_2$. The experimental broadband EELS spectrum is also reasonably captured by the loss function obtained from *ab initio* calculations, as shown in (d)–(f) for different momentum values, reported in the legend of panel (e). The 19.0 eV peak in (d) has the highest intensity in experiment as well as the *ab initio* calculations. The other dominant intraband peaks at 3.9 and 7.5 eV are resolved in panel (f).

D. Electron energy-loss spectroscopy and SAED analyses

The reflection EELS experiments were performed at room temperature by means of an EELS apparatus with two 50-mm hemispherical deflectors for both monochromator and analyzers, mounted in an ultrahigh-vacuum chamber at the University of Calabria, Italy. The primary electron beam impinges on the sample with an incident angle θ_i of 43° with respect to the surface normal, along the Γ-K direction of the surface Brillouin zone. The primary electron beam energy is $E_p = 100$ eV.

SAED and high-angle annular dark-field-scanning TEM (HAADF-STEM) and STEM-EELS analyses were carried out at room temperature on a FEI Tecnai G2 F20 TWIN TEM, equipped with a Gatan Enfinium SE spectrometer at Istituto Italiano di Tecnologia, Genoa, Italy. For these experiments a primary electron beam energy $E_p = 200$ keV and a collection angle of 13 mrad were used. Samples for TEM analyses were prepared by drop casting of the flakes dispersion onto a holey carbon-coated Cu grid. The EELS spectra were collected from flakes regions suspended on holes in the carbon support film. From the same spectra, the local thickness was evaluated using the log-ratio method [32]. The estimated inelastic free path through $PtTe_2$ in these conditions is $\lambda \approx 78$ nm.

III. THEORY

A. Energy-loss function

The theoretical calculation of the electron energy-loss function starts with the noninteracting density-density response function ($\chi^0_{\mathbf{GG}'}$) for a periodic lattice. It is obtained

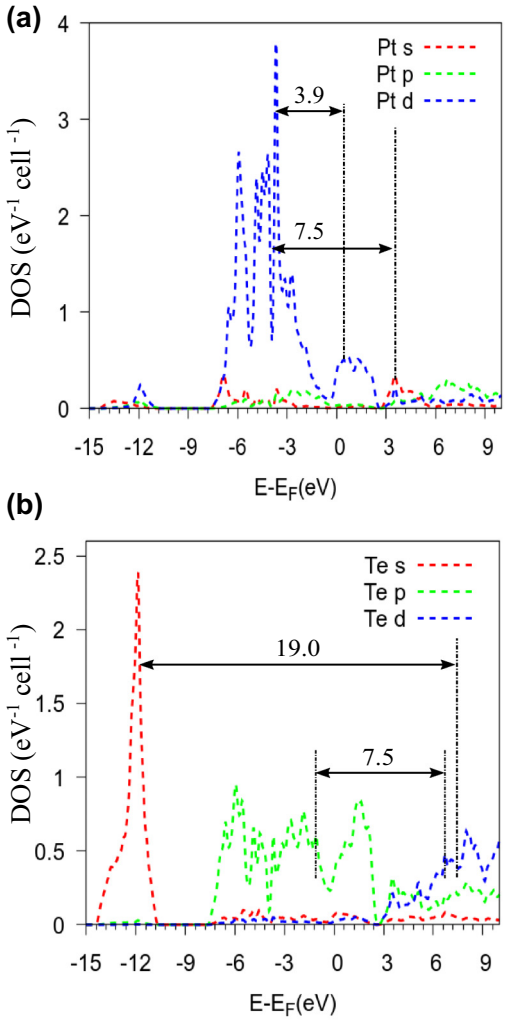

FIG. 3. Orbital-resolved density of states corresponding to (a) Pt orbitals and (b) Te orbitals. The dominant transitions, corresponding to the observed EELS peaks, are marked by arrows. The corresponding orbital-resolved band-structure plots are shown in Fig. 4.

using the Adler-Wiser formula given by [33,34]

$$\chi^0_{\mathbf{GG}'}(\mathbf{q},\omega) = \frac{1}{\Omega}\sum_{\mathbf{k}}^{\mathrm{BZ}}\sum_{n,n'}\frac{f_{n\mathbf{k}} - f_{n'\mathbf{k}+\mathbf{q}}}{\omega + \epsilon_{n\mathbf{k}} - \epsilon_{n'\mathbf{k}+\mathbf{q}} + i\eta} \times \langle\psi_{n\mathbf{k}}|e^{-i(\mathbf{q}+\mathbf{G})\cdot\mathbf{r}}|\psi_{n'\mathbf{k}+\mathbf{q}}\rangle_{\Omega_{\mathrm{cell}}}\langle\psi_{n\mathbf{k}}|e^{i(\mathbf{q}+\mathbf{G}')\cdot\mathbf{r}'}|\psi_{n'\mathbf{k}+\mathbf{q}}\rangle_{\Omega_{\mathrm{cell}}}. \quad (1)$$

The wave function $\psi_{n\mathbf{k}}$, eigenvalue $\epsilon_{n\mathbf{k}}$, and the corresponding Fermi-Dirac occupation function $f_{n\mathbf{k}}$ at wave vector $\mathbf{k}$ for the band with index n are obtained from the ground-state calculations performed using DFT.

The interacting density-density response function can be obtained within the framework of time-dependent DFT by solving a Dyson-like equation [35]. Using a plane-wave basis for a periodic system, for a given $(\mathbf{q},\omega)$, it can be expressed as

$$\chi_{\mathbf{GG}'} = \chi^0_{\mathbf{GG}'} + \sum_{\mathbf{G}_1,\mathbf{G}_2}\chi^0_{\mathbf{GG}_1}(\mathbf{q},\omega)K_{\mathbf{G}_1\mathbf{G}_2}(q)\chi_{\mathbf{G}_2\mathbf{G}'}(\mathbf{q},\omega), \quad (2)$$

where $\mathbf{G}$ and $\mathbf{q}$ are the reciprocal lattice vector and the Bloch wave vector, respectively, and $K_{\mathbf{G}_1\mathbf{G}_2}$ is the interaction kernel, including both the Coulomb or Hartree term, as well as the exchange correlations.

Using the calculated $\chi_{\mathbf{GG}'}$ matrix from Eq. (2), the inverse of the microscopic dielectric matrix, $\epsilon_{\mathbf{GG}'}(\mathbf{q},\omega)$, for a test charge in a crystal can obtained to be [36]

$$\epsilon^{-1}_{\mathbf{GG}'}(\mathbf{q},\omega) = \delta_{\mathbf{GG}'} + \frac{4\pi}{|\mathbf{q}+\mathbf{G}|^2}\chi_{\mathbf{GG}'}(\mathbf{q},\omega). \quad (3)$$

The corresponding microscopic electronic dielectric matrix is obtained by adding the exchange term in Eq. (3). The average or macroscopic dielectric constant (a complex scalar) probed in experiments is related to the (0,0) element of the inverse of the inverse microscopic dielectric matrix: $\epsilon_M(\mathbf{q},\omega) = [\mathbb{1}/\epsilon^{-1}_{\mathbf{GG}'}(\mathbf{q},\omega)]_{00}$.

The dynamical loss function, which is directly related to the experimental excitation spectrum probed by EELS, is now obtained from the macroscopic dielectric function,

$$\mathcal{E}_{\mathrm{loss}}(\mathbf{q},\omega) = -\mathrm{Im}\left[\frac{1}{\epsilon_M(\mathbf{q},\omega)}\right]. \quad (4)$$

The collective density excitations or plasmons are characterized by the zeros of the real part of the macroscopic dielectric function (the denominator of the density-density response function within random phase approximation [RPA]). Thus, they appear as peaks in the EELS spectrum. The calculations of the loss function are performed using the generalized RPA, which uses the local-field factors to add the impact of the exchange and correlation effects, in addition to the Hartree field [37].

B. Computational details

Electronic band-structure calculations were performed using a plane-wave basis set within the framework of DFT, as implemented in the VASP package [38,39]. We use the projector augmented wave pseudopotentials with 500 eV kinetic energy cutoff for the plane-wave basis set [40]. The exchange-correlation part of the potential has been treated within the framework of the generalized approximation scheme developed by Perdew-Burke-Ernzerhof [41]. Starting from the experimental structure, we relax all the atomic positions until the forces on each atom are less than 0.001 eV/Å. Spin-orbit interaction has been considered as a perturbation and treated in a self-consistent manner.

In order to calculate the response functions we use the GPAW code, which employs a real-space representation of the PAW potentials [42–44]. A kinetic energy cutoff of 500 eV has been used for the plane-wave basis set. We use a $122 \times 122 \times 20$ k grid to calculate the momentum dependence of the loss function. To incorporate the local-field effects, we use a plane-wave cutoff of 60 eV, which corresponds to 85 plane waves. A broadening parameter $\eta = 0.05$ eV is assumed in all calculations of the response function.

IV. BROADBAND SPECTRUM OF BULK $PtTe_2$

The experimental broadband EELS spectra of the $PtTe_2$ bulk sample, measured with an electron beam energy of

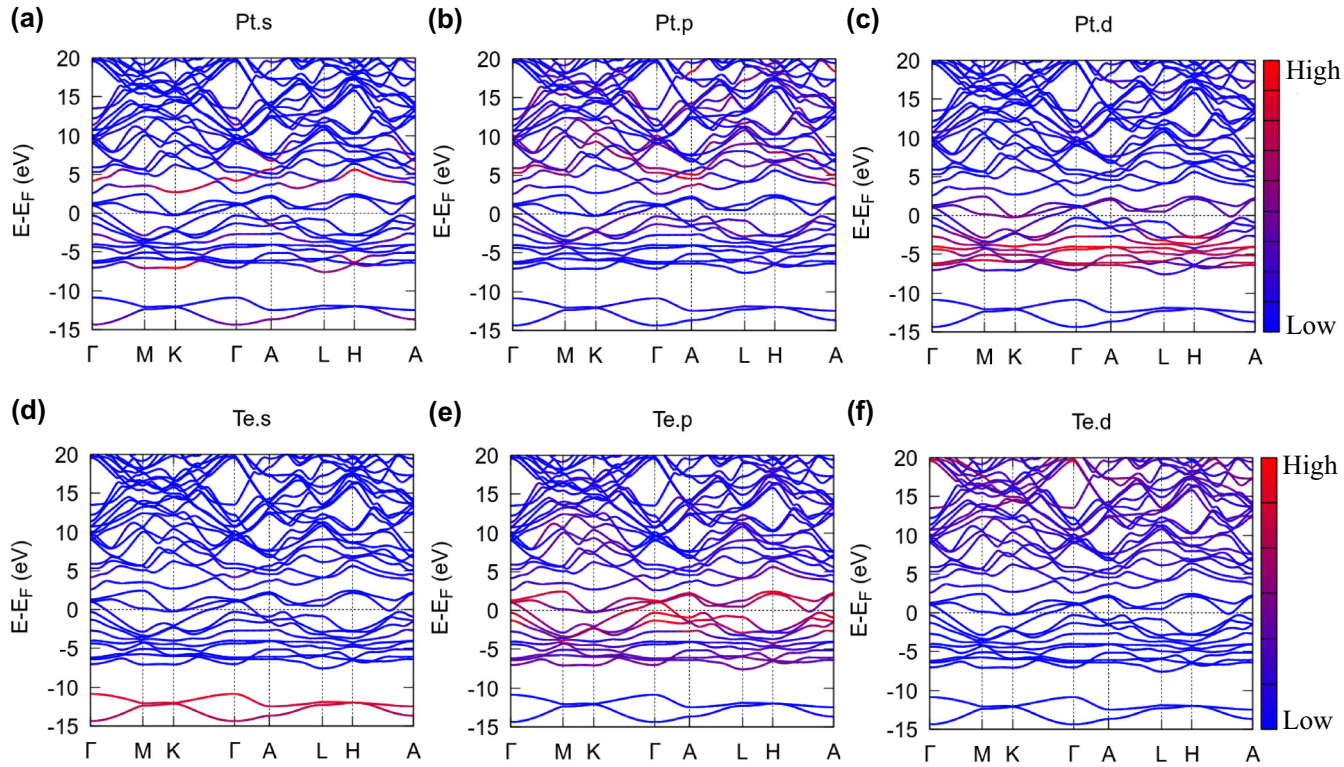

FIG. 4. Orbital-projected band structure of $PtTe_2$. The lowest energy states are dominated by the Te_{5s} orbital. Near the Fermi energy the states have major contributions from the Pt_{5d} and Te_{5p} orbitals. The higher energy states are mostly Pt_{6p} and Te_{5d} states.

100 eV, is shown in Figs. 2(a)–2(c). The broadband EELS spectrum shows distinctly resolved peaks at energies ∼0.5, ∼1.4, ∼3.9, ∼7.5, and ∼19.0 eV, among others. The lowest-energy peak at 0.5 eV is the intraband gapped three-dimensional (3D) Dirac plasmon excitation in bulk $PtTe_2$, which disperses with momentum [see Fig. 2(e)]. It has been discussed in detail in Ref. [20]. Here, we will focus on the remaining interband excitations, which are relatively less dispersive compared to the intraband 3D Dirac plasmon peak. We find that their peak location and relative intensity is nearly independent of the scattering geometry and, consequently, of the momentum in the range of $k \sim 0.0$–0.2. Å^{-1}.

The theoretical loss function in Figs. 2(d)–2(f) captures the qualitative features of the experimental excitation spectrum reasonably well. Note that the spectral amplitudes of the theoretical and experimental peaks cannot be directly compared, as the experimental features in the reflection mode EELS depend on the energy of the primary electron beam. This was shown explicitly for the case of Sb_2Te_3 recently, for which the calculated intensities were found to match with the EELS spectrum acquired in the transmission mode, and only for very high value of the impinging electron energies (∼500 eV) in the reflection mode [45–47].

In order to identify the interband transitions corresponding to the observed peaks in the EELS spectrum, we show the orbital-resolved density of states (DOS) in Figs. 3(a) and 3(b). The corresponding orbital-resolved band-structure plot is shown in Fig. 4. The energetically lower valence band (VB) is situated approximately between −15 and −10 eV and it is mostly dominated by Te_{5s} states. The upper VB extends from −7 eV up to the Fermi level and mostly comprises Pt_{5d} and Te_{5p} orbitals. The lower conduction-band states until ∼3 eV are also primarily formed by Pt_{5d} and Te_{5p} orbitals. The conduction-band states at higher energy have contributions mainly from the Pt_{6p} and Te_{5d} orbitals. A comparison of the orbital-resolved DOS with the observed spectral features in the broadband EELS spectrum allows us to identify the prominent states involved in the transitions. We find that the peaks at 3.9, 7.5, and 19.0 eV are predominantly connected to $Pt_{5d} \rightarrow Pt_{5d}$, $Te_{5p} \rightarrow Te_{5d}$, and $Te_{5s} \rightarrow Te_{5d}$ transitions, respectively, as marked by arrows in Figs. 3(a) and 3(b).

Having discussed the EELS spectrum of the bulk $PtTe_2$ crystal, we now proceed to discuss the EELS spectrum of thin $PtTe_2$ layers in the next section.

V. BROADBAND SPECTRUM OF THIN $PtTe_2$ LAYERS

In this section, we explore the thickness dependence of the broadband EELS spectrum of $PtTe_2$ thin films. To this aim, we have employed the STEM-EELS technique, which affords the spatial resolution necessary to identify regions with different thickness within the flakes. As shown in Fig. 5(a), the liquid-phase exfoliation of $PtTe_2$ has produced flakes with inhomogeneous thickness. Therefore, for STEM-EELS experiments, different thicknesses [indicated in Fig. 5(b)] were probed on different areas of the same fragments.

Our STEM-EELS investigation suggests that in $PtTe_2$ the momentum-integrated (over the collection angle) high-energy

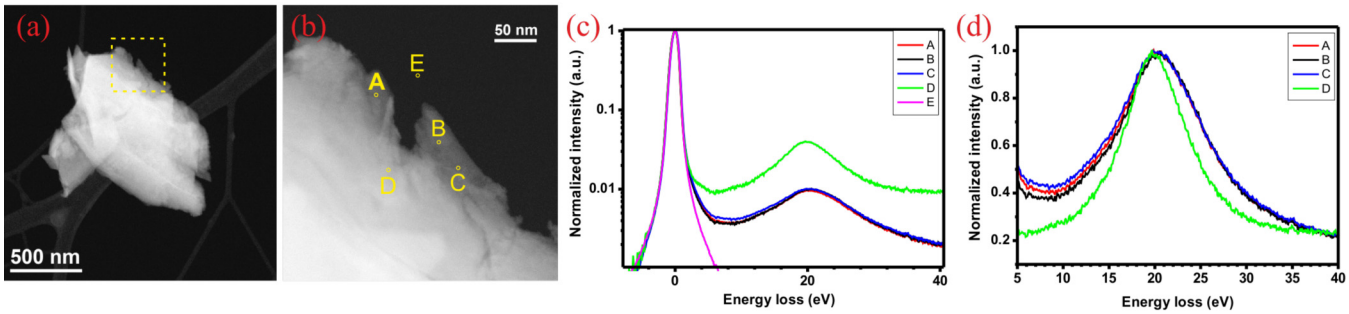

FIG. 5. High-angle annular dark-field (HAADF)-STEM image of a $PtTe_2$ flake, partially suspended on a hole in the amorphous carbon support film. The portion magnified in (b) was used for STEM-EELS analysis. The points A, B, and C exhibit a lower thickness (lower brightness in HAADF-STEM mode, corresponding to $\sim 0.2\lambda$) than point D (corresponding to $\sim 0.8\lambda$). (c) Only the zero-loss peak appears in the spectrum recorded at point E, i.e., 35 nm far from the $PtTe_2$ flake. (d) The broadband STEM-EELS spectra acquired for points A, B, C, and D. In panel (c) the intensity is normalized to the zero-loss peak maximum, while in panel (d) it is normalized to that of the peak at at ~ 20 eV, in order to highlight the dissimilarities in the line shape of the peaks corresponding to different thickness.

EELS peak changes in both line shape and energy position as a function of thickness. Specifically, an asymmetrical line shape, centered at about 23 eV [Fig. 5(c)], is recorded for thinner regions (about 30 $PtTe_2$ unit cells along the c axis), whereas a symmetrical line shape, with a corresponding centroid around 20.5 eV, is revealed for thicker regions (about 120 $PtTe_2$ unit cells along the c axis). This is in contrast to other layered materials such as graphene [29,30] and phosphorene [48]. The high-energy EELS peak in $PtTe_2$ is redshifted with increasing thickness. The change in the line shape, with an asymmetrical shape characterizing the thinner regions, is ascribable to the multiple contributions (i.e., due to regions with different thickness) to the spectra acquired in the thinner regions of the flakes. The presence of contributions from regions a few nanometers away from the position of the electron beam is due to the delocalization of inelastic scattering, prominent in the low-energy-loss range [49,50].

VI. CONCLUSIONS

We have probed the broadband excitation spectrum of bulk crystals and thin layers of $PtTe_2$, using EELS in reflection mode for bulk and STEM-EELS for thin layers. In the case of bulk $PtTe_2$ we find different modes in the ultraviolet regime at 3.9, 7.5, and 19.0 eV, in addition to the excitations associated to the 3D Dirac cones observed in the infrared range at 0.5 and 1.4 eV. These observations are well explained by the DFT-based orbital-resolved band-structure and DOS calculations. Specifically, we find that in bulk $PtTe_2$ the observed peaks at 3.9, 7.5, and 19.0 eV are predominantly connected to $Pt_{5d} \rightarrow Pt_{5d}$, $Te_{5p} \rightarrow Te_{5d}$, and $Te_{5s} \rightarrow Te_{5d}$ transitions, respectively. In thin layers, with decreasing thickness, the high-energy EELS peak gets shifted from 20.5 to 23.0 eV. This redshift with increasing thickness is in contrast to the blueshift observed in the case of graphene. Moreover, with an increasing number of layers a decrease in the asymmetry of the line shape of the high-energy plasmon peak is observed. This peculiarity can be exploited for characterizing the thickness of $PtTe_2$ thin films. Similar physics is expected to play out in other members of the family as well, including $PdTe_2$ and $PtSe_2$.

APPENDIX: VALENCE-BAND STATES IN $PtTe_2$

As an additional check we explicitly check that there are no valence-band states below the -14 eV in $PtTe_2$, by calculating the band structure over a wide energy range. The calculated band structure is shown in Fig. 6: it is evident that there are no valence-band states in $PtTe_2$ from approximately -14 to -50 eV.

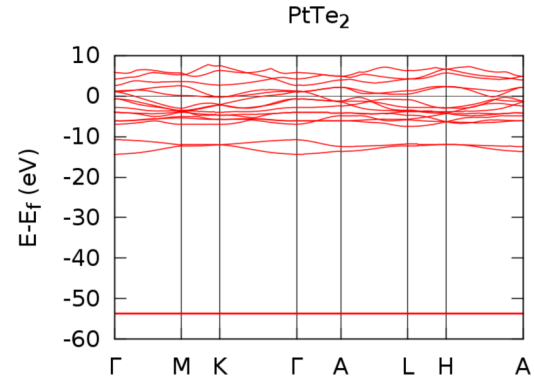

FIG. 6. Band structure of $PtTe_2$ over a wide energy region. Evidently, there are no energy states in between -13 and -50 eV.

[1] A. Castellanos-Gomez, Why all the fuss about 2D semiconductors? Nat. Photonics **10**, 202 (2016).

[2] L. Li, W. Wang, Y. Chai, H. Li, M. Tian, and T. Zhai, Few-layered PtS_2 phototransistor on h-BN with high gain, Adv. Funct. Mater. **27**, 1701011 (2017).

[3] A. A. Soluyanov, D. Gresch, Z. Wang, QuanSheng Wu, M. Troyer, X. Dai, and B. A. Bernevig, Type-II Weyl semimetals, Nature (London) **527**, 495 (2015).

[4] M. Yan, H. Huang, K. Zhang, E. Wang, W. Yao, K. Deng, G. Wan, H. Zhang, M. Arita, H. Yang, Z. Sun, H. Yao, Y. Wu, S. Fan, W. Duan, and S. Zhou, Lorentz-violating type-II Dirac fermions in transition metal dichalcogenide $PtTe_2$, Nat. Commun. **8**, 257 (2017).

[5] M. S. Bahramy, O. J. Clark, B.-J. Yang, J. Feng, L. Bawden, J. M. Riley, I. Markovic, F. Mazzola, V. Sunko, D. Biswas, S. P. Cooil, M. Jorge, J. W. Wells, M. Leandersson, T. Balasubramanian, J. Fujii, I. Vobornik, J. E. Rault, T. K. Kim, M. Hoesch, K. Okawa, M. Asakawa, T. Sasagawa, T. Eknapakul, W. Meevasana, and P. D. C. King, Ubiquitous formation of bulk Dirac cones and topological surface states from a single orbital manifold in transition-metal dichalcogenides, Nat. Mater. **17**, 21 (2017).

[6] H.-J. Noh, J. Jeong, E.-J. Cho, K. Kim, B. I. Min, and B.-G. Park, Experimental Realization of Type-II Dirac Fermions in a $PdTe_2$ Superconductor, Phys. Rev. Lett. **119**, 016401 (2017).

[7] K. Zhang, M. Yan, H. Zhang, H. Huang, M. Arita, Z. Sun, W. Duan, Y. Wu, and S. Zhou, Experimental evidence for type-II Dirac semimetal in $PtSe_2$, Phys. Rev. B **96**, 125102 (2017).

[8] H. Huang, S. Zhou, and W. Duan, Type-II Dirac fermions in the $PtSe_2$ class of transition metal dichalcogenides, Phys. Rev. B **94**, 121117 (2016).

[9] T.-R. Chang, S.-Y. Xu, D. S. Sanchez, W.-F. Tsai, S.-M. Huang, G. Chang, C.-H. Hsu, G. Bian, I. Belopolski, Z.-M. Yu, S. A. Yang, T. Neupert, H.-T. Jeng, H. Lin, and M. Z. Hasan, Type-II Symmetry-Protected Topological Dirac Semimetals, Phys. Rev. Lett. **119**, 026404 (2017).

[10] M. Kargarian, M. Randeria, and Y.-M. Lu, Are the surface Fermi arcs in Dirac semimetals topologically protected? Proc. Natl. Acad. Sci. USA **113**, 8648 (2016).

[11] M. Kargarian, Y.-M. Lu, and M. Randeria, Deformation and stability of surface states in Dirac semimetals, Phys. Rev. B **97**, 165129 (2018).

[12] X. Lin, J. C. Lu, Y. Shao, Y. Y. Zhang, X. Wu, J. B. Pan, L. Gao, S. Y. Zhu, K. Qian, Y. F. Zhang *et al.*, Intrinsically patterned two-dimensional materials for selective adsorption of molecules and nanoclusters, Nat. Mater. **16**, 717 (2017).

[13] Y. Zhao, J. Qiao, Z. Yu, P. Yu, K. Xu, S. P. Lau, W. Zhou, Z. Liu, X. Wang, W. Ji, and Y. Chai, High-electron-mobility and air-stable 2D layered $PtSe_2$ FETs, Adv. Mater. **29**, 1604230 (2017).

[14] X. Chia, A. Adriano, P. Lazar, Z. Sofer, J. Luxa, and M. Pumera, Layered platinum dichalcogenides (PtS_2, $PtSe_2$, and $PtTe_2$) electrocatalysis: Monotonic dependence on the chalcogen size, Adv. Funct. Mater. **26**, 4306 (2016).

[15] Y. Wang *et al.*, Monolayer $PtSe_2$, a new semiconducting transition-metal-dichalcogenide, epitaxially grown by direct selenization of Pt, Nano Lett. **15**, 4013 (2015).

[16] Z. Wang, Q. Li, F. Besenbacher, and M. Dong, Facile synthesis of single crystal $PtSe_2$ nanosheets for nanoscale electronics, Adv. Mater. **28**, 10224 (2016).

[17] H. Ma, P. Chen, B. Li, J. Li, R. Ai, Z. Zhang, G. Sun, K. Yao, Z. Lin, B. Zhao, R. Wu, X. Tang, X. Duan, and X. Duan, Thickness-tunable synthesis of ultrathin type-II Dirac semimetal $PtTe_2$ single crystals and their thickness-dependent electronic properties, Nano Lett. **18**, 3523 (2018).

[18] A. Ciarrocchi, A. Avsar, D. Ovchinnikov, and A. Kis, Thickness-modulated metal-to-semiconductor transformation in a transition metal dichalcogenide, Nat. Commun. **9**, 919 (2018).

[19] W. Yao, E. Wang, H. Huang, K. Deng, M. Yan, K. Zhang, K. Miyamoto, T. Okuda, L. Li, Y. Wang, H. Gao, C. Liu, W. Duan, and S. Zhou, Direct observation of spin-layer locking by local Rashba effect in monolayer semiconducting $PtSe_2$ film, Nat. Commun. **8**, 14216 (2017).

[20] A. Politano, G. Chiarello, B. Ghosh, K. Sadhukhan, C.-N. Kuo, C. S. Lue, V. Pellegrini, and A. Agarwal, 3D Dirac Plasmons in the Type-II Dirac Semimetal $PtTe_2$, Phys. Rev. Lett. **121**, 086804 (2018).

[21] F. H. L. Koppens, T. Mueller, P. Avouris, A. C. Ferrari, M. S. Vitiello, and M. Polini, Photodetectors based on graphene, other two-dimensional materials and hybrid systems, Nat. Nanotechnol. **9**, 780 (2014).

[22] X. Yu, P. Yu, D. Wu, B. Singh, Q. Zeng, H. Lin, W. Zhou, J. Lin, K. Suenaga, Z. Liu, and Q. J. Wang, Atomically thin noble metal dichalcogenide: A broadband mid-infrared semiconductor, Nat. Commun. **9**, 1545 (2018).

[23] X. Zhang, K. Wang, J. Ma, Q. Zhang, P. Yan, and X. Tian, Ultraviolet imaging based on surface plasmon resonance with azo-polymer sensing layer, IEEE Photonics Technol. Lett. **27**, 1297 (2015).

[24] J.-Y. Ou, J.-K. So, G. Adamo, A. Sulaev, L. Wang, and N. I. Zheludev, Ultraviolet and visible range plasmonics in the topological insulator $Bi_{1.5}Sb_{0.5}Te_{1.8}Se_{1.2}$, Nat. Commun. **5**, 5139 (2014).

[25] F. Bisio, R. Proietti Zaccaria, R. Moroni, G. Maidecchi, A. Alabastri, G. Gonella, A. Giglia, L. Andolfi, S. Nannarone, L. Mattera, and M. Canepa, Pushing the high-energy limit of plasmonics, ACS Nano **8**, 9239 (2014).

[26] S.-D. Guo and J.-L. Wang, Spin-orbital coupling effect on the power factor in semiconducting transition-metal dichalcogenide monolayers, Semicond. Sci. Technol. **31**, 095011 (2016).

[27] M. Rocca, Low-energy EELS investigation of surface electronic excitations on metals, Surf. Sci. Rep. **22**, 1 (1995).

[28] H. Zeng and X. Cui, An optical spectroscopic study on two-dimensional group-VI transition metal dichalcogenides, Chem. Soc. Rev. **44**, 2629 (2015).

[29] T. Eberlein, U. Bangert, R. R. Nair, R. Jones, M. Gass, A. L. Bleloch, K. S. Novoselov, A. Geim, and P. R. Briddon, Plasmon spectroscopy of free-standing graphene films, Phys. Rev. B **77**, 233406 (2008).

[30] P. Wachsmuth, R. Hambach, G. Benner, and U. Kaiser, Plasmon bands in multilayer graphene, Phys. Rev. B **90**, 235434 (2014).

[31] B. Ghosh, P. Kumar, A. Thakur, Y. S. Chauhan, S. Bhowmick, and A. Agarwal, Anisotropic plasmons, excitons, and electron energy loss spectroscopy of phosphorene, Phys. Rev. B **96**, 035422 (2017).

[32] T. Malis, S. C. Cheng, and R. F. Egerton, EELS log-ratio technique for specimen-thickness measurement in the TEM, Microsc. Res. Tech. **8**, 193 (1988).

[33] S. L. Adler, Quantum theory of the dielectric constant in real solids, Phys. Rev. **126**, 413 (1962).

[34] N. Wiser, Dielectric constant with local field effects included, Phys. Rev. **129**, 62 (1963).

[35] W. Hanke and L. J. Sham, Local-field and excitonic effects in the optical spectrum of a covalent crystal, Phys. Rev. B **12**, 4501 (1975).

[36] M. S. Hybertsen and S. G. Louie, *Ab initio* static dielectric matrices from the density-functional approach. I. Formulation and application to semiconductors and insulators, Phys. Rev. B **35**, 5585 (1987).

[37] G. Giuliani and G. Vignale, *Quantum Theory of the Electron Liquid*, Masters Series in Physics and Astronomy (Cambridge University Press, Cambridge, UK, 2005).

[38] W. Kohn and L. J. Sham, Self-consistent equations including exchange and correlation effects, Phys. Rev. **140**, A1133 (1965).

[39] G. Kresse and J. Furthmüller, Efficient iterative schemes for *ab initio* total-energy calculations using a plane-wave basis set, Phys. Rev. B **54**, 11169 (1996).

[40] G. Kresse and D. Joubert, From ultrasoft pseudopotentials to the projector augmented-wave method, Phys. Rev. B **59**, 1758 (1999).

[41] J. P. Perdew, K. Burke, and M. Ernzerhof, Generalized Gradient Approximation Made Simple, Phys. Rev. Lett. **77**, 3865 (1996).

[42] J. J. Mortensen, L. B. Hansen, and K. W. Jacobsen, Real-space grid implementation of the projector augmented wave method, Phys. Rev. B **71**, 035109 (2005).

[43] J. Enkovaara *et al.*, Electronic structure calculations with GPAW: A real-space implementation of the projector augmented-wave method, J. Phys.: Condens. Matter **22**, 253202 (2010).

[44] S. R. Bahn and K. W. Jacobsen, An object-oriented scripting interface to a legacy electronic structure code, Comput. Sci. Eng. **4**, 56 (2002).

[45] I. A. Nechaev, I. Aguilera, V. De Renzi, A. di Bona, A. Lodi Rizzini, A. M. Mio, G. Nicotra, A. Politano, S. Scalese, Z. S. Aliev, M. B. Babanly, C. Friedrich, S. Blügel, and E. V. Chulkov, Quasiparticle spectrum and plasmonic excitations in the topological insulator Sb_2Te_3, Phys. Rev. B **91**, 245123 (2015).

[46] A. Politano, V. Formoso, and G. Chiarello, Interplay between single-particle and plasmonic excitations in the electronic response of thin Ag films, J. Phys.: Condens. Matter **25**, 305001 (2013).

[47] V. U. Nazarov, Multipole surface-plasmon-excitation enhancement in metals, Phys. Rev. B **59**, 9866 (1999).

[48] R. J. Wu, M. Topsakal, T. Low, M. C. Robbins, N. Haratipour, J. S. Jeong, R. M. Wentzcovitch, S. J. Koester, and K. A. Mkhoyan, Atomic and electronic structure of exfoliated black phosphorus, J. Vacuum Sci. Technol. A **33**, 060604 (2015).

[49] C. C. Ahn, *Transmission Electron Energy Loss Spectrometry in Materials Science and the EELS Atlas* (Wiley-VCH, Weinheim, 2004).

[50] R. F. Egerton, *Electron Energy-Loss Spectroscopy in the Electron Microscope*, Language of science (Plenum, New York, 1996).